PROCEEDINGS OF SCIENCE

Front-End Computational Modeling and Design for the Antarctic Demonstrator for the Advanced Particle-astrophysics Telescope

Marion Sudvarg,[a,*] **Ye Htet,**[a] **Roger Chamberlain,**[a] **Jeremy Buhler,**[a] **Blake Bal,**[b] **Corrado Altomare,**[c] **Davide Serini,**[c] **Mario Nicola Mazziotta,**[c] **Leonardo Di Venere,**[c] **Wenlei Chen**[d] **and James Buckley**[b] **for the APT collaboration**

[a] *Washington University in St. Louis, Department of Computer Science & Engineering, St. Louis, MO, USA*
[b] *Washington University in St. Louis, Department of Physics & McDonnell Center for the Space Sciences, St. Louis, MO, USA*
[c] *Istituto Nazionale di Fisica Nucleare, Sezione di Bari, Bari, Italy*
[d] *University of Minnesota, Department of Physics and Astronomy, Minneapolis, MN, USA*
E-mail: msudvarg@wustl.edu, htet.ye@wustl.edu, roger@wustl.edu, jbuhler@wustl.edu, corrado.altomare@ba.infn.it, davide.serini@ba.infn.it, b.bal@wustl.edu, marionicola.mazziotta@ba.infn.it, Leonardo.Divenere@ba.infn.it, chen6339@umn.edu, buckley@wustl.edu

The Advanced Particle-astrophysics Telescope (APT) is a planned space-based observatory designed to localize MeV to TeV transients such as gamma-ray bursts in real time using onboard computational hardware. The Antarctic Demonstrator for APT (ADAPT) is a prototype high-altitude balloon mission scheduled to fly during the 2025–26 season. Gamma-ray-induced scintillations in CsI tiles will be captured by perpendicular arrays of optical fibers running across both tile surfaces, as well as SiPM-based *edge detectors* to improve light collection and calorimetry. Signal samples are captured by analog waveform digitizer ASICs then sent to the front end of the computational pipeline, which is designed to be deployed on a set of FPGAs.

This paper presents a model for uncertainty in the measured positions and deposited energies of Compton scatters in ADAPT, informed by simulations of the scintillation response and optical propagation properties of the CsI tiles, as well as existing characterizations of the SiPM and preamplifier boards. Anisotropic background radiation and event pileup are also considered. We describe our current implementation of event processing and data reduction for individual gamma rays, including both pedestal subtraction and signal integration. Preliminary work shows that high-level synthesis (HLS) enables the logic for pedestal subtraction and signal integration across 96 ASIC channels to run in 302 clock cycles on a single Kintex-7 FPGA. This demonstrates the feasibility of using FPGA hardware to accelerate the front-end event-building stage prior to back-end reconstruction and localization.

38th International Cosmic Ray Conference (ICRC2023)
26 July - 3 August, 2023
Nagoya, Japan

*Speaker

PoS(ICRC2023)764

1. Introduction

The Advanced Particle-astrophysics Telescope (APT) is a planned space-based observatory designed for MeV to TeV gamma-ray astrophysics and cosmic-ray physics. APT's multimessenger capability relies on its ability to localize MeV transients in real time using on-board computational hardware. APT will combine a pair tracker and Compton telescope in a single monolithic design to include multiple layers of scintillating-fiber tracker hodoscopes and sodium-doped CsI scintillators. The CsI tiles are coupled with crossed planes of wavelength-shifting (WLS) fibers to localize energy deposition to ~mm accuracy, as well as SiPM-based edge detectors to improve light collection and calorimetry. At ICRC 2021, we presented the mission concept [1], instrument simulations [2], and real-time GRB reconstruction and localization algorithms [3].

The Antarctic Demonstrator for APT (ADAPT) is a prototype high-altitude balloon mission scheduled to fly during the 2025–26 season. ADAPT will demonstrate APT's pair and Compton detection capabilities while serving as a proof of concept for prompt Compton reconstruction and localization, with the ability to send GRB positional alerts in real time. To estimate ADAPT's performance, we have developed a simulated model of the instrument that incorporates optical properties of its CsI tiles, measurements of WLS signal attenuation, as well as characterizations of the SiPMs and preamplifier boards. Our model also captures the additional uncertainty caused by the temporal effects of signal integration, including tail loss and event pileup.

In this paper, we provide an overview of the current design of the ADAPT instrument and its front-end electronics, focusing on those properties relevant to Compton-regime event detection. We describe the optical simulations that inform a model of light captured by the edge detectors from scintillations in the CsI crystal. We additionally present the current model of light propagation and transmission through the WLS fibers, using lab measurements of signal attenuation as a function of transmission distance. We summarize existing characterizations of the SiPMs and preamplifier boards to estimate dark-count rates and electronic noise. We also detail the effects of the current design of front-end analog waveform digitizers, signal integration, and triggering logic on signal loss and event pileup. Refinements to our Compton reconstruction and localization algorithms and their performance for GRBs simulated under our new model are presented at this year's ICRC [4].

This paper also updates on the status of front-end data reduction. Preliminary work shows that high-level synthesis (HLS) enables the logic for pedestal subtraction and signal integration across 96 ASIC channels to fit on a single Kintex-7 FPGA with sufficient throughput to handle a high sustained event rate. These results demonstrate HLS as a viable and flexible approach to accelerating the front-end event-building stages prior to back-end localization and acceleration.

2. ADAPT Design Overview

The ADAPT instrument (illustrated in Fig. 1a) has 4 primary detector layers, each comprised of an imaging CsI Calorimeter (ICC) and scintillating fiber tracker. Each ICC consists of a 3×3 arrangement of 5 mm thick, 15×15 cm sodium-doped CsI scintillating crystal tiles. Optical photons produced by energy deposits in the crystals are captured by perpendicular arrays of 2 mm wavelength-shifting (WLS) optical fibers running across the top and bottom surfaces of the CsI tiles and terminated at one end with 3×3 mm SiPMs; these allow precise localization of interactions in

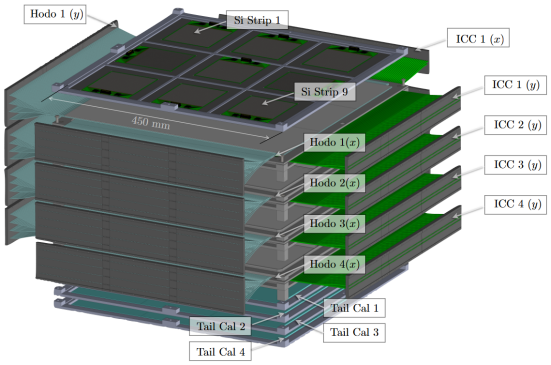

(a) The ADAPT detector stack.

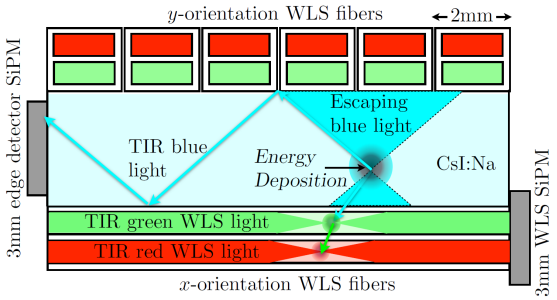

(b) A single ICC layer, illustrating totally internally reflected (TIR) optical light propagation and detection.

Figure 1: The ADAPT instrument [1].

the crystals. To improve light detection and energy estimates, a detector that multiplexes 36 SiPMs (illustrated in Fig. 2) is placed over each of the 6 tile edges on the adjacent ICC sides opposite the WLS fiber SiPMs. Below the ICC layers are 4 closely-spaced tail counters, which are identical to the ICCs but lack WLS fiber arrays, making them useful only for calorimetry.

WLS fiber SiPM outputs are combined across a tile-width span (3-fiber multiplexing) into a SMART shaping preamplifier ASIC channel [5]. SMART outputs are sampled and digitized by a 16-channel ALPHA ASIC, a successor to the TARGET series [6]. The signals from all 36 SiPMs in an edge detector array are passively combined into both low- and high-gain preamplifier stages, each of which are also sampled by a dedicated ALPHA channel. The ALPHA ASIC captures 256×10 ns samples per channel in dual-banked analog memory, allowing simultaneous sampling and readout when triggered. Values are digitized and sent to an FPGA over a shared bus.

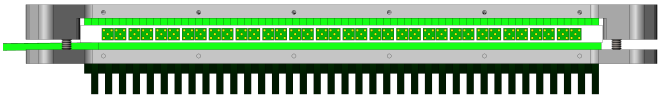

Figure 2: Side view of a single CsI tile, with orthogonal WLS fibers and 36 edge detector SiPMs illustrated.

With 225 WLS fibers running along each axis of an ICC layer, 5 ALPHA ASICs are sufficient to capture a single layer-axis. A sixth ALPHA will capture edge detector signals, with channels remaining open for other uses (e.g., capturing edge detectors from tail counter layers). A single Kintex 7 FPGA handles communication from the 6 ALPHAs for a layer-axis, then performs pedestal subtraction, signal integration, zero-suppression, and island detection. Both FPGAs send integrals to a third FPGA for each layer that performs centroiding and event building. Centroids are then sent to a CPU for backend data analysis, including Compton reconstruction and GRB localization [4].

3. Edge Detector Model

We performed dedicated GEANT4-based optical simulations of an ICC layer to create position- and energy-dependent distributions of optical photons captured by the edge SiPMs. These are integrated into our complete instrument simulation, which in combination with the SiPM photon detection efficiency (PDE) can be used to model the number of optical photons detected without running a full optical simulation for every scintillation. Our simulation incorporates the production and propagation of optical photons, allowing us to optimize the ge-

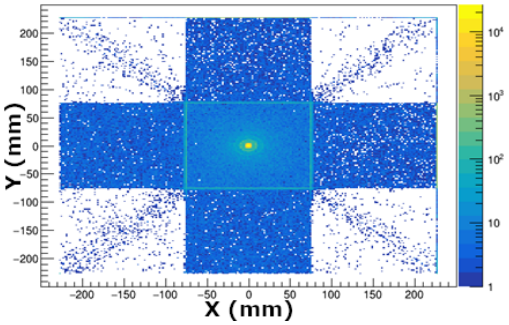

Figure 3: Photon absorption positions from a point-like energy release at the ICC center.

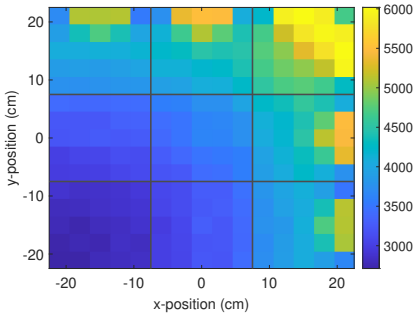

(a) Map of scintillation position to photons per MeV, with detectors placed on top and right tile edges.

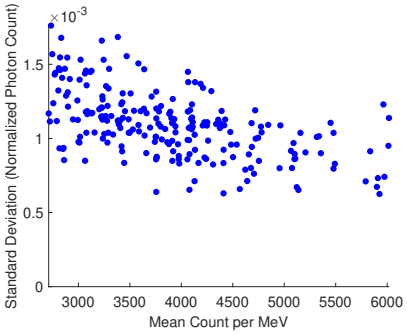

(b) Optical photon standard deviations.

Figure 4: Optical photon edge absorption results.

ometric and optical properties of the detector, as well as the design of the readout system. We assigned a refractive index of 1.84 to the crystal and a scintillation yield of 41 000 photons/MeV using the Saint-Gobain CsI(Na) emission spectrum. Additionally, we consider a 1 mm thick epoxy glue layer with a refractive index of 1.41 at the surface between two adjacent tiles, and we include a silicone window around the edges of the entire detector. Two edges are treated as perfect reflective surfaces, while the other two edges act as perfect absorbers (SiPM-like sensors). WLS fibers with a square cross section are implemented in the global geometry, with users able to customize fiber characteristics such as dimensions and cladding thickness [7]. All individual optical photons are tracked inside the detector volumes, and those reaching the interface between two different materials are propagated according to Snell's law. We simulated point-like energy deposits (500 keV) across the entire detector area with a step of 3 cm (5×5 points per tile), and 20 deposits per position. Absorption information (material and position) for each optical photon was saved (Fig. 3).

These simulation results inform position-dependent distributions of optical photons captured by the edge detectors. We mapped the positions of each tracked optical photon to determine which would be absorbed by a SiPM instead of escaping through the gaps illustrated in Fig. 2, obtaining a mean incident count per MeV for each of the 125 simulated positions. For a scintillation in the CsI crystal, we use the expected value, scaled to the deposited energy, from the closest of these positions (Fig. 4a). To obtain a standard deviation, we normalized each incident photon count across all 4 500 optical simulations to the aggregate mean, then found the standard deviation at each position. Results are plotted against the expected counts in Fig. 4b. As there is no strong correlation between expected count and normalized standard deviation, we use the standard deviation across all normalized samples. For an energy deposit in the ICC layer, the complete instrument simulator samples from a distribution using the position-dependent, energy-scaled mean and a standard deviation of 0.0158 times the mean value per MeV, scaled by the square root of the energy. Each captured optical photon is detected according to the SiPM's PDE. We use a Hamamatsu S14160-3050HS, for which the datasheet reports a PDE of 50%. However, the lab measurements presented in Fig. 7b of [8] suggest that a similar SiPM may have a slightly lower PDE for the blue light produced by the CsI(Na) crystal scintillators; we use a more conservative estimate of 45%.

4. WLS Fiber Characterization

Signal Attenuation: We model the WLS fiber response to photons produced by the CsI scintillator using similar assumptions as in [2]: an energy deposit in the CsI(Na) crystal produces optical

photons per its light yield. These are propagated in the "bowtie" pattern illustrated in Fig. 1b, then a constant transmission efficiency determines the fraction piped to the end of the WLS fibers. Unlike the prior work, our new simulator models attenuation loss as a function of distance. To measure this effect, we placed a WLS fiber in an optical rail with ports to accommodate an LED flasher spaced at 10 cm intervals. The end of the fiber was centered on a single 3 mm SiPM/preamp module.

By using an oscilloscope to measure the SiPM response to 395 nm flashes at each port, we obtained a mean pulse height for distances up to 125 cm from the fiber end. To eliminate variations in the output of the pulse generator over the course of testing, we also obtained the mean pulse height from a SiPM on a separate fiber mounted on a stand and illuminated by the LED at a distance of 31 cm. Our test values, normalized to this standardization measurement, are plotted in Fig. 5.

The attenuation shows a rapid fall-off near the fiber end, followed by a much slower drop-off at large distances. We fit an exponential distribution with y-offset to these measurements (Fig. 5, "Exponential Fit"). Since the SiPM ends of the fibers extend 20 cm past the edge of the CsI crystal, we consider distances from 20–65 cm ("CsI Adjacency Range"). APTSoft's transmission efficiency was obtained as an average over lab measurements across several positions, so we normalize our attenuation function to its value at 42.5 cm ("Normalized Attenuation"). Our new model scales the prior estimate of photon transmission according to the formula $a = 0.8789e^{-0.02126d} + 0.4615$, where d is the distance in centimeters from the edge of the tile, and a is the attenuation factor.

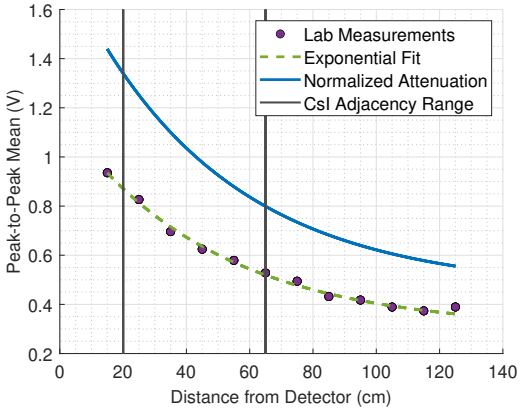

Figure 5: WLS fiber signal attenuation.

SiPM Photon Detection Efficiency: We use the same SiPMs for the WLS fibers as the edge detectors. The lab measurements presented in Fig. 7b of [8] suggest a slightly higher PDE for the green light produced by the fibers, so we use a value of 50%. To determine the number of photons captured by each WLS fiber for a given scintillation signal, we select from a Poisson distribution with a mean determined by the attenuated estimate multiplied by the PDE. While this model still lacks absolute calibrations of optical efficiencies, it provides a reasonable estimate.

5. Electronic Noise Characterization

SiPM Dark Counts: These are estimated according to the lab measurements presented in Fig. 22b of [8]. At a relative overvoltage of ~5%, and with SiPMs cooled to 10°C, the dark-count rate is around 70 kHz for a single 3×3 mm SiPM. As 3 WLS fibers are multiplexed into a single SMART/ALPHA channel, then sampled every 10 ns, we assume an estimated rate of 0.0021 per sample. For the edge detectors, we aggregate the dark count across all 216 SiPMs in a layer, for an estimated rate of 0.1512 per sample. Our simulator samples the dark count from a Poisson distribution given the expected rate over an integration window.

SMART Preamplifier Noise: To characterize a baseline noise level, we sampled the ADC counts from a single SMART preamplifier channel. As illustrated in Fig. 6a, the RMS noise per ns was

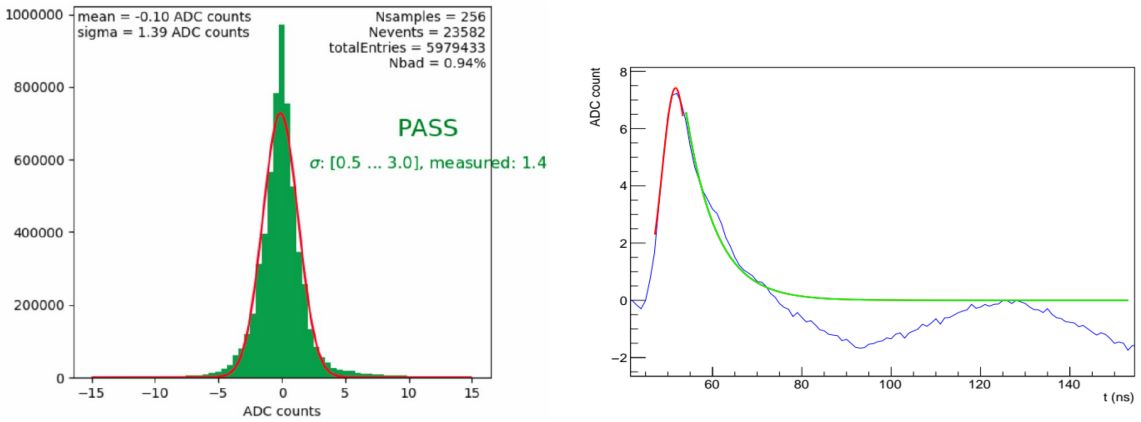

(a) SMART Preamplifier RMS Noise. **(b)** SMART Single-PE Impulse Response.

Figure 6: SMART preamplifier characteristics.

determined to be $\sigma = 1.39$. To estimate the affects of multiplexing, we scale this value by $\sqrt{3}$ for the WLS fibers and $\sqrt{216}$ for the edge detectors, then further scale to the signal integration time.

The SMART's single-PE impulse response is illustrated in Fig. 6b. We model the first 13 ns with a Gaussian function centered at 10 ns and use an exponential falloff for the last 27 ns. We ran a Monte Carlo simulation to find the distribution of ADC counts produced by a single-PE impulse response. For each trial, we generated parameters for the function from normal distributions obtained by lab measurements, then found the resulting total ADC count when sampled at 1 ns intervals. Over 10^7 trials, the mean and standard deviation were found to be 88.6 and 5.57 respectively.

Signal Integration: We model the arrival curve for optical photons produced by a scintillation in the CsI crystal as an exponential distribution with a mean of 633 ns. At present, we assume perfect triggering: the first sample sent by each ALPHA ASIC for integration on the FPGA corresponds to exactly the time that the scintillation occurred. Then for some integration window T, the expected number of photons detected must be scaled by the area under the exponential distribution in $t \in [0, T]$. Our simulator samples the actual number detected by sampling from a binomial distribution with a probability equal to this area (scaled by the SiPM's PDE for the edge detectors). This imposes a tradeoff on the size of the integration window: a higher probability of capture decreases the capture variance, but increases the preamplifier noise and dark count. By modeling this tradeoff, we selected a 1.5 μs integration window for the edge detectors and 2.5 μs for the WLS fiber signals; both are within the 2.56 μs capacity of each ALPHA channel.

Event Pileup: We simulate GRBs with individual gamma-ray photon arrival times sampled from a normal distribution. These, in addition to events triggered by the anisotropic background radiation from the Earth's limb (which we also model for ADAPT at this year's ICRC [9]), may pile up; i.e., signals from multiple events may be captured within the same ALPHA readout window. To simulate this for a given burst, we assume that a trigger occurs at exactly the time of the first event. Any events arriving within the integration window have signals captured according to the proportion of the optical photon arrival curve that lies within the remaining integration window. The first event arriving after a 3 μs holdoff time from the previous trigger triggers the next readout; we currently assume that the tails of events arriving within the holdoff window are insufficient to cause the next trigger. However, any events occurring within 1.9 μs prior to a trigger have their corresponding tail signals added to the readout (after 1.9 μs, less than 5% of the tail density remains).

6. High-Level Synthesis of FPGA Logic

Table 1: HLS FPGA Utilization Results.

Impl.	FFs	%	LUTs	%	BRAM	%	*II*
(1)	30 954	7.6	71 988	35.3	450	50.6	275
(2)	27 864	6.8	60 372	29.6	540	60.7	269

We have implemented pedestal subtraction and integration using HLS, targeting a Kintex 7 XC7K325T FPGA. 12-bit unsigned sampled ADC values from a single ALPHA are vectorized across the 16 channels, enabling SIMD processing. Pipelined dataflow execution further improves throughput. Pedestal values for each analog memory unit on the ALPHA are vectorized and stored in block RAM (BRAM). Samples are integrated using 4 sets of bounds to capture different components of the signal arrival curve, although at present only a single integration window (with values described in § 5) is used for island detection and centroiding. We have considered two different implementations of the integration logic: (1) uses a separate parallel logic block for each integral, adding the current sample if its index is within the corresponding bounds; and (2) sequentially computes a single prefix sum, then computes each integral by subtracting prefix sum values at indices corresponding to the integral bounds.

Performance and utilization estimates reported by the Vitis HLS tools across 6 ALPHA ASICs are reported in Tbl. 1. Even with a conservatively slow 100 MHz clock, both versions have a sufficiently low initiation interval (*II*) to support sustained event arrivals every 3 μs, the fastest that can be achieved due to the triggering holdoff. And even for 6 ALPHA ASICs, the FPGA remains underutilized, although subsequent zero-suppression and island detection have not yet been profiled. We presented a preliminary assessment of centroiding using HLS in [10], requiring only 68 cycles to centroid a typical island. However, we have not yet synthesized the new centroiding techniques described in [4]; updated performance estimates will be given in future work.

7. Conclusions and Unmodeled Behavior

In this paper, we have described updates to our simulated model of the ADAPT detector instrument to include characterizations of its optical properties, front-end electronics, and the temporal effects of signal integration and event pileup. Event data produced under this model are used to analyze the Compton reconstruction and GRB localization performance of both ADAPT and the future full APT instrument in [4].

However, a full detector model is still under development. We have primarily considered scintillations in the CsI crystal; however, gamma rays and other particles can interact directly in the tracker and WLS fibers. Such interactions are still simulated according to [2]; we do not yet introduce additional uncertainty due to dark counts, electronic noise, and signal integration. Additionally, we model all interactions using the same signal arrival curves; the shorter timescale of scintillations directly in the WLS fibers has not yet been captured in our pileup model. Further, we presently use simulator ground truth to distinguish interactions directly in the WLS fibers from photons captured from CsI scintillations. This may often be valid due to the different timescales and signal distributions involved (an interaction directly in a fiber typically produces a signal only in that fiber), but has not been verified.

The effects of multiplexing 3 WLS fibers into a single ALPHA channel also needs more consideration. While we do scale SiPM dark counts and electronic noise to account for multiplexing,

we currently assume that signals can be attributed to the appropriate fiber. As Fig. 3 suggests, the distribution of signals across edge detectors may be used to localize scintillations to tile-level resolution, which in turn determines the corresponding fiber. However, more complex scenarios (such as events producing multiple interactions at different locations in the same layer) still need to be addressed. Further, our model currently assumes perfect zero-suppression in WLS fibers that do not capture scintillated light. It also remains to better characterize the distribution of captured light; measurements from our smaller prototype APTlite instrument [11] and newer optical simulations suggest that the "bowtie" model may not be realistic. Finally, our models for electronic noise are produced by scaling measurements taken from a single SMART preamplifier channel; lab measurements to characterize the noise from 3× and 36× multiplexed SiPMs, as well as calibrations of optical efficiencies, are ongoing.

This paper has also described our current HLS-based implementation of the FPGA logic used to accelerate front-end data reduction and event processing. Results suggest the feasibility of using these techniques to achieve the necessary throughput demanded by the maximum triggering rate while staying within the available area of the target FPGA. Synthesis of pedestal subtraction, island detection, and the newer centroiding techniques discussed in [4] are still in progress.

References

[1] J. Buckley et al., *The Advanced Particle-astrophysics Telescope (APT) Project Status*, in *Proc. of 37th Int'l Cosmic Ray Conference*, vol. 395, pp. 655:1–655:9, July, 2021, DOI.

[2] W. Chen et al., *The Advanced Particle-astrophysics Telescope: Simulation of the Instrument Performance for Gamma-Ray Detection*, in *Proc. of 37th Int'l Cosmic Ray Conference*, vol. 395, pp. 590:1–590:9, 2021, DOI.

[3] M. Sudvarg et al., *A Fast GRB Source Localization Pipeline for the Advanced Particle-astrophysics Telescope*, in *Proc. of 37th Int'l Cosmic Ray Conference*, vol. 395, pp. 588:1–588:9, July, 2021, DOI.

[4] Y. Htet, M. Sudvarg, J. Buhler, R. Chamberlain, W. Chen, J.H. Buckley et al., *Prompt and Accurate GRB Source Localization Aboard the Advanced Particle Astrophysics Telescope (APT) and its Antarctic Demonstrator (ADAPT)*, in *Proc. of 38th Int'l Cosmic Ray Conference*, vol. 444, pp. 956:1–956:9, July, 2023, DOI.

[5] C. Aramo, E. Bissaldi, M. Bitossi et al., *A SiPM multichannel ASIC for high Resolution Cherenkov Telescopes (SMART) developed for the pSCT camera telescope*, *Nucl. Instrum. Methods Phys. Res. A* **1047** (2023) 167839.

[6] K. Bechtol, S. Funk, A. Okumura, L. Ruckman, A. Simons, H. Tajima et al., *TARGET: A multi-channel digitizer chip for very-high-energy gamma-ray telescopes*, *Astroparticle Physics* **36** (2012) 156.

[7] D. Serini et al., *Simulation of a Compton-pair imaging calorimeter and tracking system for the next generation of MeV gamma-ray telescopes*, *Journal of Physics: Conference Series* **2374** (2022) 012116.

[8] A.N. Otte, D. Garcia, T. Nguyen and D. Purushotham, *Characterization of three high efficiency and blue sensitive silicon photomultipliers*, *Nucl. Instrum. Methods Phys. Res. A* **846** (2017) 106.

[9] W. Chen, J. Buckley et al., *Simulation of the instrument performance of the Antarctic Demonstrator for the Advanced Particle-astrophysics Telescope in the presence of the MeV background*, in *Proc. of 38th Int'l Cosmic Ray Conference*, vol. 444, pp. 841:1–841:9, July, 2023, DOI.

[10] J. Wheelock et al., *Supporting multi-messenger astrophysics with fast gamma-ray burst localization*, in *Proc. of IEEE/ACM HPC for Urgent Decision Making Workshop (UrgentHPC)*, Nov., 2021, DOI.

[11] Z. Hughes et al., *Characterization of a prototype imaging calorimeter for the Advanced Particle-astrophysics Telescope from an Antarctic balloon flight and CERN beam test*, in *Proc. of 37th Int'l Cosmic Ray Conference*, vol. 395, pp. 137:1–137:9, July, 2021, DOI.

Full Authors List: APT Collaboration

Marion Sudvarg[2], Ye Htet[2], Roger D. Chamberlain[2], Jeremy Buhler[2], Blake Bal[7], Corrado Altomare[12], Davide Serini[12], Mario Nicola Mazziotta[12], Leonardo Di Venere[12], Wenlei Chen[6], James H. Buckley[7], Ulysses Atkeson[2], Meagan Konst[2], Thomas Lang[2], Shun Li[2], Diana Pacheco-Garcia[2], Nick Song[2], Chenfeng Zhao[2], Zhiting Zhou[2], Matthew Andrew[5], Richard G. Bose[7], Dana Braun[7], Eric Burns[4], Michael L. Cherry[4], Jeffrey Dumonthier[13], Manel Errando[7], Stefan Funk[10], Priya Ghosh[8], Francesco Giordano[9], Jonah Hoffman[7], Zachary Hughes[7], Aera Jung[5], Patrick L. Kelly[6], John F. Krizmanic[13], Makiko Kuwahara[3], Francesco Licciulli[12], Gang Liu[16], Leonarda Lorusso[9], John Grant Mitchell[11], John W. Mitchell[1], Georgia A. de Nolfo[11], Giuliana Panzarini[15], Richard Peschke[5], Riccardo Paoletti[17], Roberta Pillera[15], Brian Rauch[7], Garry Simburger[7], George Suarez[13], Teresa Tatoli[11], Gary S. Varner[5], Eric A. Wulf[14], Adrian Zink[10], and Wolfgang V. Zober[7]

[1]Astroparticle Physics Laboratory, NASA/GSFC, Greenbelt, MD 20771, USA. [2]Department of Computer Science & Engineering, Washington University, St. Louis, MO 63130-4899, USA. [3]Department of Engineering, University of Hawai'i at Mānoa, Honolulu, HI 96822, USA. [4]Department of Physics and Astronomy, Louisiana State University, Baton Rouge, Louisiana 70803, USA. [5]Department of Physics and Astronomy, University of Hawai'i at Mānoa, Honolulu, HI 96822, USA. [6]Department of Physics and Astronomy, University of Minnesota, Minneapolis, MN 55455, USA. [7]Department of Physics and McDonnell Center for the Space Sciences, Washington University, St. Louis, MO 63130, USA. [8]Department of Physics, Catholic University of America, Washington DC, 20064. [9]Dipartimento di Fisica "M. Merlin" dell'Università e del Politecnico di Bari, I-70126 Bari, Italy. [10]Friedrich-Alexander-Universität Erlangen-Nürnberg, Erlangen Centre for Astroparticle Physics, D-91058 Erlangen, Germany. [11]Heliospheric Physics Laboratory, NASA/GSFC, Greenbelt, MD 20771, USA. [12]Istituto Nazionale di Fisica Nucleare, Sezione di Bari, I-70126 Bari, Italy. [13]NASA Goddard Space Flight Center, Greenbelt, MD 20771, USA. [14]Naval Research Laboratory, Washington, DC 20375, USA. [15]Politecnico di Bari, Department of Mechanics, Mathematics and Management, via Orabona, 4, I-70125 Bari, Italy. [16]SLAC National Accelerator Laboratory, 2575 Sand Hill Rd, Mailstop 0094, Menlo Park, CA 94025, USA. [17]Università di Siena and INFN Pisa, I-53100 Siena, Italy.

Acknowledgments

This work was supported by NASA award 80NSSC21K1741 and NSF award CNS-1763503.